Acoustic Radiation from a Mach 14 Turbulent Boundary layer

Chao Zhang* and Lian Duan†

Missouri University of Science and Technology, Rolla, MO 65409

Meelan M. Choudhari‡

NASA Langley Research Center, Hampton, VA 23681

Direct numerical simulations (DNS) are used to examine the turbulence statistics and the radiation field generated by a high-speed turbulent boundary layer with a nominal freestream Mach number of 14 and wall temperature of 0.18 times the recovery temperature. The flow conditions fall within the range of nozzle exit conditions of the Arnold Engineering Development Center (AEDC) Hypervelocity Tunnel No. 9 facility. The streamwise domain size is approximately 200 times the boundary-layer thickness at the inlet, with a useful range of Reynolds number corresponding to $Re_\tau \approx 450 - 650$. Consistent with previous studies of turbulent boundary layer at high Mach numbers, the weak compressibility hypothesis for turbulent boundary layers remains applicable under this flow condition and the computational results confirm the validity of both the van Driest transformation and Morkovin's scaling. The Reynolds analogy is valid at the surface; the RMS of fluctuations in the surface pressure, wall shear stress, and heat flux is 24%, 53%, and 67% of the surface mean, respectively. The magnitude and dominant frequency of pressure fluctuations are found to vary dramatically within the inner layer ($z/\delta \lessapprox 0.08$ or $z^+ \lessapprox 50$). The peak of the pre-multiplied frequency spectrum of the pressure fluctuation is $f\delta/U_\infty \approx 2.1$ at the surface and shifts to a lower frequency of $f\delta/U_\infty \approx 0.7$ in the free stream where the pressure signal is predominantly acoustic. The dominant frequency of the pressure spectrum shows a significant dependence on the freestream Mach number both at the wall and in the free stream.

Nomenclature

C_p	heat capacity at constant pressure, J/(K·kg)
C_v	heat capacity at constant volume, J/(K·kg)
H	shape factor, $H = \delta^*/\theta$, dimensionless
M	Mach number, dimensionless
Pr	Prandtl number, $Pr = 0.71$, dimensionless
R	ideal gas constant, $R = 287$, J/(K·kg)
Re_θ	Reynolds number based on momentum thickness and freestream viscosity, $Re_\theta \equiv \frac{\rho_\infty U_\infty \theta}{\mu_\infty}$, dimensionless
Re_{δ_2}	Reynolds number based on momentum thickness and wall viscosity, $Re_{\delta_2} \equiv \frac{\rho_\infty U_\infty \theta}{\mu_w}$, dimensionless
Re_τ	Reynolds number based on shear velocity and wall viscosity, $Re_\tau \equiv \frac{\rho_w u_\tau \delta}{\mu_w}$, dimensionless
rms	root mean square
T	temperature, K

*Graduate Student, Student Member, AIAA

†Assistant Professor, Member, AIAA

‡Aerospace Technologist, Computational AeroSciences Branch, M.S. 128. Associate Fellow, AIAA

T_r recovery temperature, $T_r = T_\infty(1 + 0.89 * \frac{\gamma-1}{2} M_\infty^2)$, K
U_∞ freestream velocity, m/s
a speed of sound, m/s
p pressure, Pa
u streamwise velocity, m/s
u_τ friction velocity, m/s
v spanwise velocity, m/s
w wall-normal velocity, m/s
x streamwise direction of the right-hand Cartesian coordinate
y spanwise direction of the right-hand Cartesian coordinate
z wall-normal direction of the right-hand Cartesian coordinate
z_τ viscous length, $z_\tau = \nu_w/u_\tau$, m
γ specific heat ratio, $\gamma = C_p/C_v$, dimensionless
δ boundary layer thickness, m
δ^* displacement thickness, m
κ thermal conductivity, $\kappa = \mu C_p/Pr$, W/(m·K)
θ momentum thickness, m
μ dynamic viscosity, $\mu = 1.458 \times 10^{-6} \frac{T^{3/2}}{T+110.4}$, kg/(m·s)
ρ density, kg/m^3

Subscripts

i inflow station for the domain of direct numerical simulations
rms root mean square
w wall variables
∞ freestream variables
t stagnation quantities

Superscripts

$+$ inner wall units
$\overline{(\cdot)}$ averaged variables
$(\cdot)'$ perturbation from averaged variable

I. Introduction

The elevated freestream disturbance levels in conventional (i.e., noisy) high-speed wind tunnels usually result in an earlier onset of transition relative to that in a flight environment or in a quiet tunnel. Yet, the conventional facilities continue to be used for transition sensitive measurements because of the size and Reynolds number limitations of existing quiet facilities and the prohibitive cost of flight tests. To enable a better use of transition data from the conventional facilities, it is important to understand the acoustic fluctuation field that dominates the freestream disturbance environment in those facilities. With increased knowledge of the receptivity mechanisms of high-speed boundary layers,[1,2] it becomes particularly important to characterize the details of the tunnel acoustics originating from the tunnel-wall turbulent boundary layers.

Direct numerical simulations (DNS) of the acoustic fluctuation field can overcome a number of difficulties encountered during experimental measurements of tunnel freestream disturbances and also provide access to quantities that cannot be measured easily.[3–5] The DNS can also isolate the acoustic radiation due to individual physical mechanisms, thereby avoiding any contamination due to secondary sources such as vortical and entropy fluctuations in the incoming stream. Successful application of DNS for capturing the freestream acoustic pressure fluctuations has been demonstrated for Mach 2.5 and Mach 6 boundary layers by the present authors.[6–8] Previous measurements suggest, however, that the Mach number scaling is greatly modified at Mach numbers that are greater than 10.[9] To understand the wind tunnel acoustic environment at the higher flow speeds and to provide insights into the disturbance spectrum and amplitude scaling with respect to the freestream Mach number, the previous computations[6–8] must be extended to a larger value of Mach number.

In this paper, we present DNS results of a spatially-developing, Mach 14, cold-wall turbulent boundary layer, with the freestream and wall-temperature conditions representative of those at the nozzle exit of the Arnold Engineering Development Center (AEDC) Hypervelocity Tunnel No. 9 facility.[10] In order to explore the correlation between the freestream pressure disturbances and the acoustic sources within the boundary

layer that give rise to the radiation field, both the hydrodynamic boundary layer and the near field of acoustic fluctuations radiated by the boundary layer need to be adequately resolved in the DNS. This paper focuses on an initial assessment of the turbulence physics within the hydrodynamic layer, including the global turbulence statistics, the fluctuating wall signals (such as wall pressure p_w, wall shear stress τ_w, and surface heat flux q_w) and the freestream disturbances. So far, there is only limited data for compressible turbulent boundary layers in the high-Mach-number, cold-wall regime.[11] Duan et al.[12,13] conducted DNS of adiabatic-wall turbulent boundary layers with varying freestream Mach numbers (up to Mach 12) and Mach 5 turbulent boundary layers with varying wall temperatures. In their study, turbulence scaling relations based on the weak compressibility hypothesis as well as the possible effects of the intrinsic compressibility were assessed. Given the temporal nature of their DNS with a periodic boundary condition in the streamwise direction as well as the limited streamwise and spanwise domain sizes, it was not possible to collect large enough turbulence ensembles to ensure the convergence of some of the high-order turbulence statistics. Priebe and Martin[14] simulated a spatially-developing hypersonic turbulent boundary layer at $M_\infty = 7.2$ with a long streamwise simulation box ($L_x = 60\delta_i$ to study the evolution of boundary-layer parameters and basic statistics as functions of streamwise distance. Although particle image velocimetry (PIV) is becoming feasible to provide global measurements of the velocity fluctuations and Reynolds stresses, the application of PIV to hypersonic boundary layers with M_∞ significantly greater than 5 remains an emerging technology.[15–17] The current DNS of a spatially-developing turbulent boundary layer with a combination of higher freestream Mach number and colder wall temperature than previous studies thus extends the available database to a more extreme yet practical case that would also allow one to assess the effects of intrinsic compressibility and the validity of the Morkovin's Hypothesis under these conditions.

The paper is structured as follows. The flow conditions selected for numerical simulation and the numerical method used are outlined in Section II. Section III is focused on the global flow structures. Section IV presents the statistical and spectral analysis of the turbulence statistics, fluctuating wall quantities, and freestream disturbances. A summary of the overall findings is given in Section V.

II. Flow Conditions and Numerical Methodology

DNS is performed for a zero-pressure-gradient turbulent boundary layer with a nominal freestream Mach number of 14 and a wall temperature ratio of $T_w/T_r \approx 0.18$ (referred to as Case M14Tw018). The selected flow conditions are representative of those at the nozzle exit of the Arnold Engineering Development Center (AEDC) Hypervelocity Tunnel No. 9 facility[10] with a total pressure of approximately 80 MPa and a total temperature of 1810 K. Relevant flow conditions are summarized in Table 1.

Table 1. Nominal freestream conditions for the DNS of a Mach 14 DNS of turbulent boundary layer (Case M14Tw018).

M_∞	U_∞(m/s)	ρ_∞(kg/m^3)	T_∞(K)	T_w(k)	P_t(Kpa)	T_t(K)	Re_{unit} $(1/m)$	$\delta_i(mm)$
14	1882.68	0.015	45.0	300	79842.0	1809.3	9.97×10^6	18.8

A. Governing Equations and Numerical Methods

The full three-dimensional compressible Navier-Stokes equations in conservation form are solved numerically. The working fluid is assumed to be a perfect gas and the usual constitutive relations for a Newtonian fluid are used: the viscous stress tensor is linearly related to the rate-of-strain tensor, and the heat flux vector is linearly related to the temperature gradient through the Fourier's law. The coefficient of viscosity μ is computed from the Sutherlands's law, and the coefficient of thermal conductivity κ is computed from $\kappa = \mu C_p/Pr$, with the molecular Prandtl number $Pr = 0.71$. A detailed description of the governing equations can be found in Wu et al.[18]

The inviscid fluxes of the governing equations are computed using a seventh-order weighted essentially non-oscillatory (WENO) scheme. Compared with the original finite-difference WENO introduced by Jiang and Shu,[19] the present scheme is optimized by means of limiters[18,20] to reduce the numerical dissipation. Both an absolute limiter on the WENO smoothness measurement and a relative limiter on the total variation are employed simultaneously during the simulation. The viscous fluxes are discretized using a fourth-order

central difference scheme and time integration is performed using a third-order low-storage Runge-Kutta scheme.[21]

B. Computational domain and simulation setup

Figure 1 shows the general computational set-up for Case M14Tw18. The DNS simulation is carried out in two stages involving overlapping streamwise domains. The domain size for Box 1 computations is ($133.3\delta_i$, $12.2\delta_i$, $55.5\delta_i$) in the streamwise, spanwise, and wall-normal directions, respectively, where δ_i represents the mean boundary layer thickness based on $u/U_\infty = 0.99$ at the inflow boundary of Box 1. The inflow boundary condition for Box 1 simulations is prescribed by means of a recycling-rescaling method adapted from Xu and Martin.[22] The original rescaling method is modified by adding the dynamic translation operations[23] to improve low-frequency characteristics of the generated inflow turbulence and by including a freestream filter to remove artificial freestream acoustics at the inlet of the computational domain introduced due to the coupling between the recycling and inflow plane.[6] This removal of recycled fluctuations in the free stream ensures that the freestream acoustic disturbances within the domain are radiated entirely from the boundary-layer turbulence rather than convected downstream from the artificial inflow.

The rescaling station is located at a distance of $100\delta_i$ downstream of the inflow station of Box 1 as indicated in Figure 1. The selected rescaling length is similar to the range of the optimum recycling length of approximately $30\delta_i$ to $99\delta_i$ as suggested by Simens et al.[24] to accommodate the eddy decorrelation length and to minimize inlet transient as a result of the recycling process. At every time step in the Box-1 DNS, the flow data on four spanwise-wall normal planes surrounding $x/\delta_i = 127.7$ are saved. As shown in Figure 1, the saved flow data are used to prescribe the inflow boundary condition for a Box-2 DNS. The data are required on four planes to satisfy the boundary condition requirement of the selected WENO scheme. At runtime for the Box-2 DNS, the saved inflow data are spline-interpolated in space and time onto the Box-2 DNS grid and to the instants dictated by the time stepping in the Box-2 DNS. The Box-2 DNS is conducted in order to further minimize any artificial effects of the rescaling procedure and to increase the streamwise extent and Reynolds-number range of the DNS. The domain size for Box 2 DNS is ($76.6\delta_i$, $12.2\delta_i$, $55.5\delta_i$) in the streamwise, spanwise, and wall-normal directions, respectively, bringing the combined streamwise extent of the full simulation (Box-1 DNS + Box-2 DNS) to approximately $194.2\delta_i$.

For both Box-1 and Box-2 DNS, the grid points are uniformly spaced in the streamwise and spanwise directions with grid spacings of $\Delta x^+ = 9.36$ and $\Delta y^+ = 4.67$, respectively. Unless otherwise stated, the grid resolutions given in this section are normalized by the viscous length scale z_τ at a plane in the downstream portion of Box-2 DNS ($x/\delta_i = 189.2$) where the turbulence statistics are collected. The grids in the wall-normal direction are clustered in the boundary layer with $\Delta z^+ = 0.47$ at the wall, and kept uniform with $\Delta z^+ = 5.68$ in the free stream until up to approximately 4.2δ, where δ is the boundary-layer thickness at ($x/\delta_i = 189.2$) and $\delta \approx 3.43\delta_i$. Such grids are designed to adequately resolve both the boundary layer and the near field of acoustic fluctuations radiated by the boundary layer. The number of grid points of the Box-1 DNS in the streamwise, spanwise, and wall-normal directions are 2500, 460, 540, respectively, and the Box 2 simulation is performed on a grid consisting of $1500 \times 460 \times 786$ in the streamwise, spanwise, and wall-normal directions. The computational grid resolution inside the boundary layer is comparable to those reported in the literature in the context of previous simulations of turbulent wall-bounded flows using comparable numerical algorithms.[12,13,25,26] The time step is selected to be $\Delta t^+ = 0.0986$ based on the stability constraints of the explicit time advancement scheme. The time step is small enough that the temporal resolution of the computed solution is not expected to be a limiting factor for its accuracy.

The initial flow field for the present DNS is generated according to the method of Martin.[25]Except for the inflow, the same boundary conditions are used in the Box-1 and Box-2 DNS. A no-slip isothermal boundary condition is specified at the wall with $T_w = 300$ K, which is approximately equal to $T_w/T_r = 0.18$. At the top and outlet boundaries, unsteady non-reflecting boundary conditions based on Thompson[27] are imposed. Periodic boundary conditions are used in the spanwise direction.

The details of the DNS methodology have been documented in our previous simulations of acoustic radiation by turbulent boundary layers.[6–8] The DNS solver has been previously shown to be suitable for computing transitional and fully turbulent flows, including hypersonic turbulent boundary layers,[12,25] the propagation of linear instability waves in 2D high-speed boundary layers, and secondary instability and laminar breakdown of swept-wing boundary layers.[28,29]

Figures 2a, 2b, and 2c show that the streamwise evolution of the boundary-layer thickness δ, the displacement thickness δ^*, and the Karman number Re_τ. Both the boundary-layer thickness and the displacement

thickness increase by a factor of more than three across the length of the simulation domain. Correspondingly, the Karman number increases from approximately 200 at the inlet to 650 at the outlet with a useful range of $Re_\tau = 450 - 650$ where the boundary layer has recovered from the initial transient due to the recycling method.

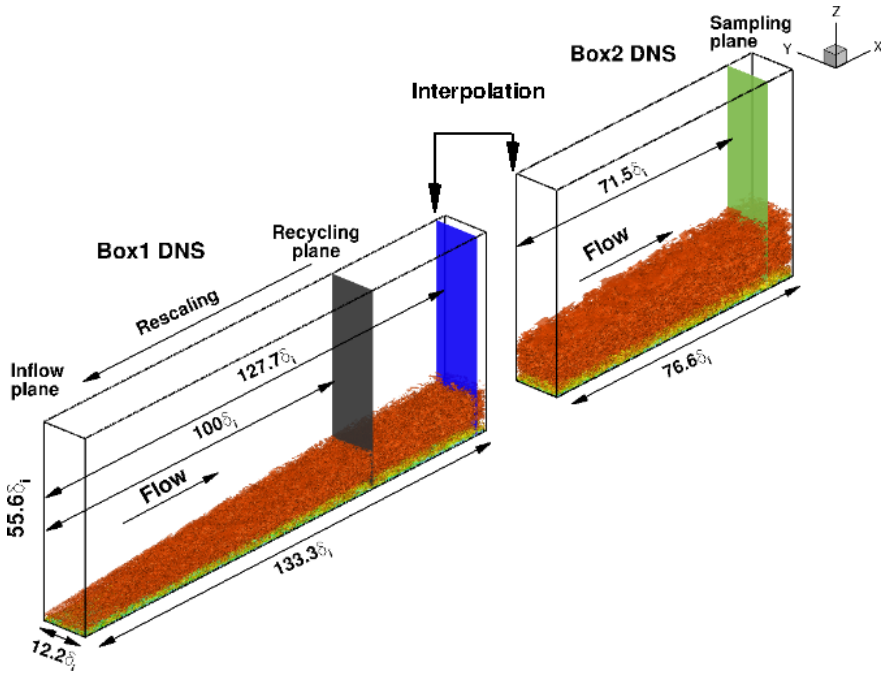

Figure 1. Computational domain and simulation setup for M14. The reference length δ_i is the thickness of the boundary layer (based on 99% of the freestream velocity) at the inlet of the Box-1 DNS. An instantaneous flow is shown in the domain, visualized by iso-surface of the magnitude of density gradient, $|\Delta\rho|\delta_i/\rho_\infty = 0.9825$, colored by the streamwise velocity component (with levels from 0 to U_∞, blue to red).

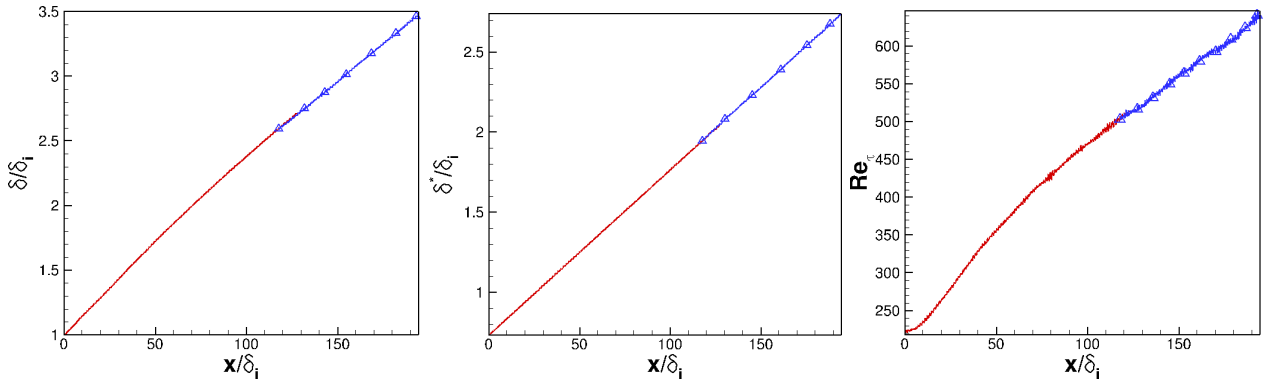

Figure 2. Evolution of boundary-layer parameters with streamwise distance (a) δ/δ_i; (b) δ^*/δ_i; (c) Re_τ. The red and blue curves represent, respectively, box 1 and box 2 of the DNS.

III. General Flow Structure

Figure 1 shows a volumetric visualization of an instantaneous flow for Case M14Tw018. The visualization shows that the boundary layer undergoes substantial growth through the computational domain: the boundary-layer thickness nearly triples from the inlet to the outlet of the domain. Figure 3 plots planar cuts

of the 'numerical Schlieren' visualization of an instantaneous flow field. The contours show the magnitude of the gradient of density, $|\nabla\rho|$, scaled using an exponential function $NS = 0.8\exp(-10|\nabla\rho|/|\nabla\rho|_{max})$ that highlights the full range of values. Large scale motions (LSMs) with turbulent eddies of size $O(\delta)$ are visible in the outer portion of the boundary layer. The LSMs cause incursions of the irrotational flow from the free stream into the rotational boundary-layer flow. The wall-ward extent of entrainment seems to span a significant portion of the boundary layer indicating a large region of intermittency. In addition, spatially distributed regions of strong density gradient can be clearly seen within the boundary layer, which indicates the existence of eddy shock waves or 'shocklets'. The appearance of shocklets is consistent with the large values of M_t and M'_{rms} as seen later in the paper. In the free stream just above the boundary layer, the instantaneous field exhibits a 'Mach-wave' radiation patten with a preferred range of wave-front inclinations.

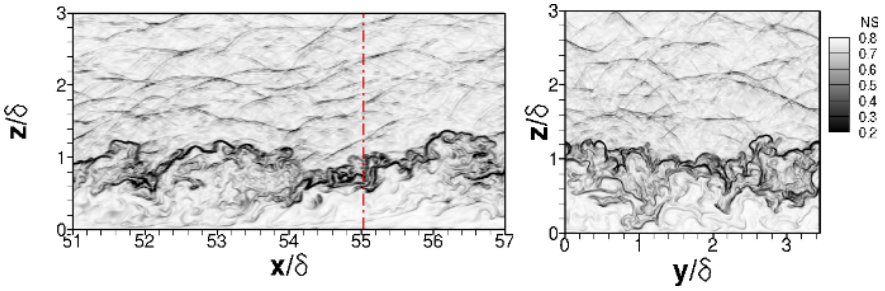

Figure 3. Numerical Schlieren visualization of a typical flow field for Case M14Tw018 in a streamwise wall-normal (x-z) plane and a spanwise wall-normal (y-z) plane. The contour levels are selected to emphasize events of strong density gradient for eddy-shocklet detection. The y-z plane is located at $x/\delta = 55$ (or $x/\delta_i = 188.9$) as indicated by the vertical dashed line.

IV. Statistical and Spectral Analysis

In the results that follow, turbulence statistics derived from the computed data are presented. Table 2 lists the values of the mean boundary layer parameters at the downstream location ($x_a = 189\delta_i$) selected for statistical analysis. Averages are first calculated over a streamwise window of $[x_a - 2.6\delta_i, x_a + 2.6\delta_i]$ and the entire spanwise extent of each instantaneous flow field; then, an ensemble average over flow field snapshots spanning a time interval of more than $279.4\delta_i/U_\infty$ is calculated.

To assess the dependence of boundary-layer statistics and the radiation field on Mach number and wall temperature, previous DNS of Mach 2.5 and Mach 6 boundary layers by the present authors[6–8] are also included. The conditions for Case M2.5 are modeled after one of the first simulations of a supersonic turbulent boundary layer by Guarini et al.[30] The flow conditions for Case M6Tw076 are similar to the operational conditions of the noisy runs of the Purdue Mach 6 Quiet Tunnel,[5,31] corresponding to a wall temperature ratio of $T_w/T_r \approx 0.76$. Case M6Tw025 has the same freestream conditions and Reynolds number Re_τ as Case M6Tw076 but a lower wall temperature ($T_w/T_r \approx 0.25$). Relevant flow conditions of these previous simulations are also summarized in Table 2.

Power spectra are calculated using the Welch method[32] with eight segments and 50% overlap. A Hamming window is used for weighting the data prior to the fast Fourier transform (FFT) processing. The sampling frequency corresponds to $f_s \approx 67U_\infty/\delta_i$ (or, equivalently, $\Delta t^+ \approx 0.099$) and the duration of an individual segment corresponds to $t_{segment} \approx 43\delta_i/U_\infty$ (i.e., $t^+_{segment} = 282$).

Table 2. Boundary layer properties at the station selected for the analysis for various DNS cases.

Case	M_∞	T_w/T_r	Re_θ	Re_τ	Re_{δ_2}	$\theta(mm)$	H	$\delta(mm)$	$z_\tau(mm)$	$u_\tau(m/s)$
M14Tw018	14	0.18	13151.9	633.07	2285.69	1.319	37.3	64.56	0.1026	67.46
M2p5	2.5	1.0	2834.8	509.9	1656.9	0.583	4.14	7.69	0.015	40.6
M6Tw076	5.86	0.76	9470.3	493.8	1869.4	0.951	11.4	25.9	0.052	45.1
M6Tw025	5.86	0.25	2080.2	480.2	2431.2	0.201	8.32	3.84	0.008	33.8

A. Boundary Layer Statistics

The van-Driest transformed mean velocity, defined as

$$\bar{u}_{VD} = \frac{1}{\bar{u}_\tau} \int_0^U (\overline{\rho}/\overline{\rho}_w)^{1/2} dU$$

is shown in Figure 4. The mean velocity shows a logarithmic region where $\overline{u}_{VD} = \frac{1}{\kappa}\log(z^+) + C$ upon van Driest transformation. Although the log region for all the DNS profiles has the same slope with $\kappa = 0.41$, there is a slight dependence of the additive constant C on the Mach number and the wall temperature conditions. As the Mach number and wall temperature conditions change, C varies from a value of $C = 5.2$ for Case M2p5 up to $C = 6.1$ for Case M14018. For comparison, in a large-domain spatially-developing DNS of a Mach 7.2 turbulent boundary layer with $T_w/T_r = 0.53$, Priebe and Martin[14] reported values of $\kappa = 0.41$ and $C = 5.9$. In terms of the Mach number and wall temperature dependence of C, Maeder[33] reported different values of C of 5.1 and 7.6, respectively, for a Mach 4.5 turbulent boundary layer with an adiabatic wall ($T_w/T_r \approx 1$) and a cold wall $T_w/T_r \approx 0.24$ while the same slope of $\kappa = 0.40$ fits his DNS data. Duan et al.[13] observed a similar but smaller variation in C for turbulent boundary layers at Mach 5 with varying wall-temperature conditions. For DNS cases with a cold wall (Cases M6Tw025 and M14Tw018), $u^+_{VD} = z^+$ is only satisfied until $z^+ \approx 2$ while for Cases M6Tw076 and M2p5 it is satisfied until $z^+ \approx 8$. This is caused by the large gradient of mean fluid properties at the wall, where the rapid change in μ and ρ prevents the relation $\mu\partial u/\partial z = \tau_w$ from being integrated to get $u^+_{VD} = z^+$ except very close to the wall.[13]

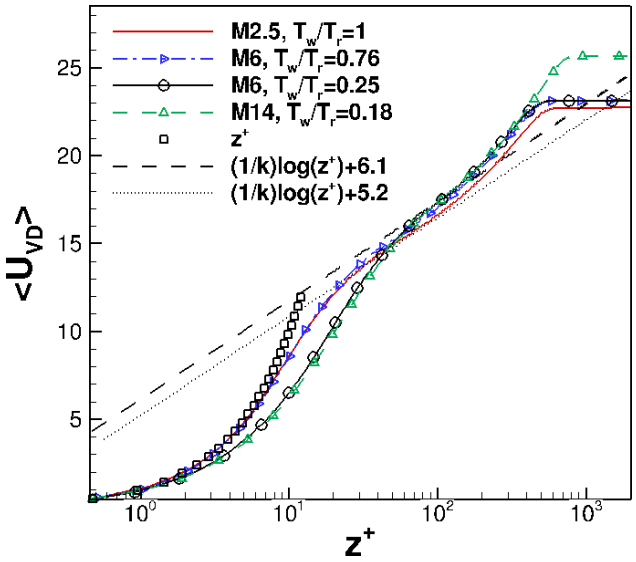

Figure 4. The van Driest transformed mean velocity profile.

Figures 5(a-f) plot turbulence intensities and density weighted turbulence intensities in streamwise, spanwise and wall-normal directions across the boundary layer for the different DNS cases. For comparison, the incompressible results by Spalart[34] and the compressible boundary layer results at Mach 4.5[35] and Mach 5[13] have also been plotted. A significantly improved collapse of data is achieved by Morkovin's scaling, which takes into account the variation in mean flow properties. Morkovin's scaling brings the magnitudes of the extrema in the compressible cases closer to the incompressible ones of Spalart,[34] but the compressible peak values are higher than the incompressible ones, as also observed by multiple researchers.[12,13,36,37]

Figure 6 shows the profiles of rms pressure fluctuation plotted against the wall-normal coordinate scaled by the local boundary layer thickness δ. For Case M14Tw018, p'_{rms}/τ_w undergoes a rapid reduction in magnitude near the wall ($z/\delta \lessapprox 0.08$ or $z^+ \lessapprox 50$), with $p'_{rms}/\tau_w \approx 4.4$ at the surface and $p'_{rms}/\tau_w \approx 2.3$ at $z/\delta \approx 0.08$ ($z^+ \approx 50$). The magnitude of pressure fluctuation nearly plateaus for $0.08 \lessapprox z/\delta \lessapprox 0.3$. As it moves farther away from the wall, the pressure fluctuation intensity decays less rapidly with the wall-normal distance before it asymptotes to a nearly constant value of $p'_{rms}/\tau_w \approx 1.2$ in the free stream for $z/\delta \gtrapprox 2.2$. Similar variation in p'_{rms}/τ_w with z/δ is seen for Case M6Tw025.

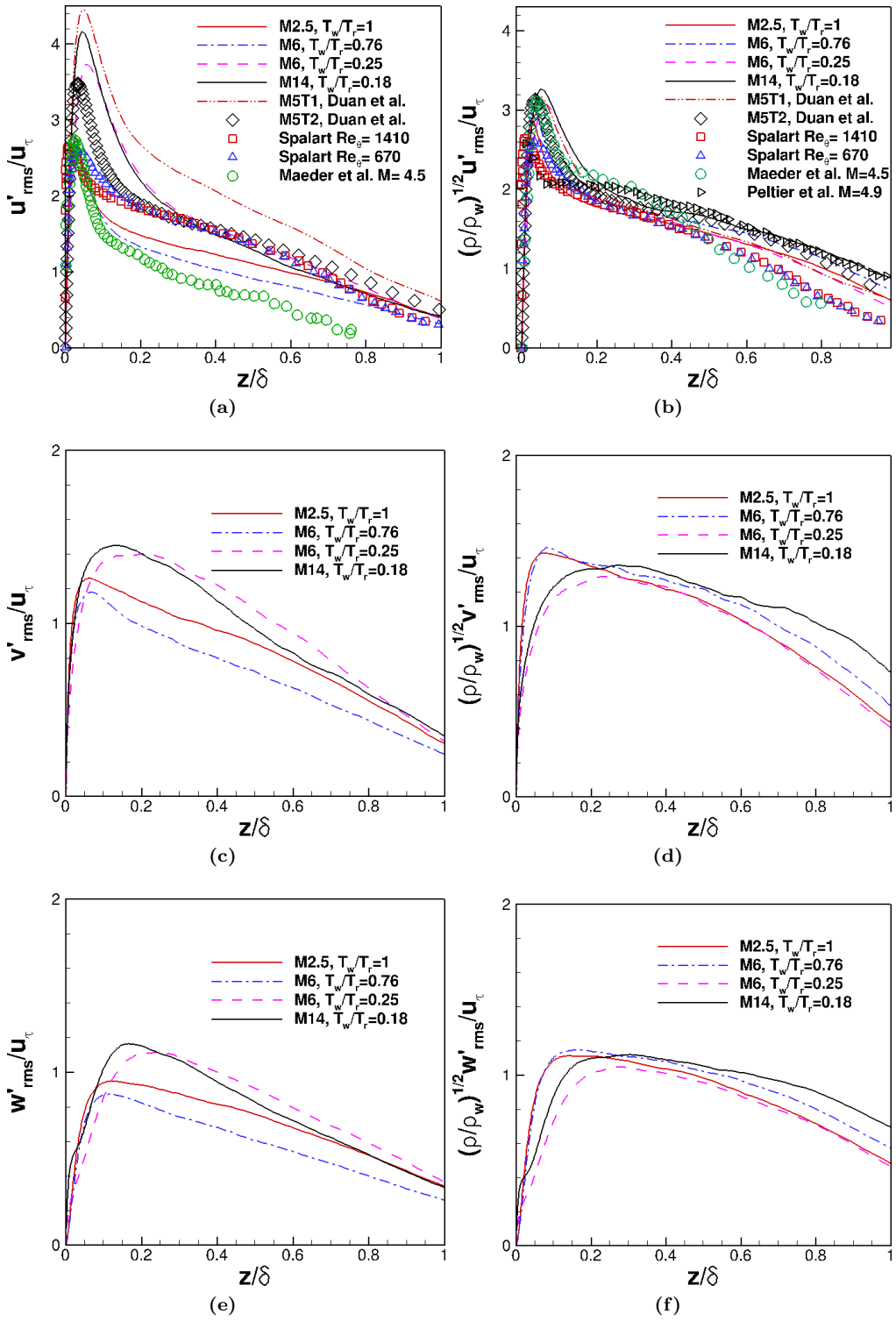

Figure 5. Turbulence intensities and density-weighted turbulence intensities of the (a,b) streamwise, (c,d) spanwise and (e,f) wall-normal fluctuating velocity components. ———: M2p5, $M_\infty = 2.5$, $Re_\theta = 2835$, $T_w/T_r = 1.0$; –·–·–: M6Tw076, $M_\infty = 6$, $Re_\theta = 9470$, $T_w/T_r = 0.76$. – – –: M6Tw025, $M_\infty = 6$, $Re_\theta = 2080$, $T_w/T_r = 0.25$. ———: M14Tw018, $M_\infty = 14$, $Re_\theta = 13152$, $T_w/T_r = 0.18$. –·–·–: M5T1,[13] $M_\infty = 5$, $Re_\theta = 1279$, $T_w/T_r = 0.18$. ◇: M5T2,[13] $M_\infty = 5$, $Re_\theta = 2300$, $T_w/T_r = 0.35$. □, Spalart,[34] $M_\infty \approx 0$, $Re_\theta = 1410$. △, Spalart,[34] $M_\infty \approx 0$, $Re_\theta = 670$. ◯, Maeder,[35] $M_\infty = 4.5$, $Re_\theta = 3305$. ▷, Peltier,[38] $M_\infty = 4.9$, $Re_\theta \approx 40 \times 10^3$.

For Cases M2p5 and M6Tw076, however, a similarly rapid reduction in the magnitude of pressure fluctuation close to the wall is not observed. Instead, the maximum of p'_{rms}/τ_w is located away from the wall at $z/\delta \approx 0.08$ ($z^+ \approx 25$) in these cases. The large difference in p'_{rms} close to the wall between boundary layers with a cold wall (Cases M14Tw018 and M6Tw025) and those with a nearly adiabatic wall (Cases M2p5 and M6Tw076) indicate a strong influence of wall-temperature conditions on the pressure fluctuation near the wall.

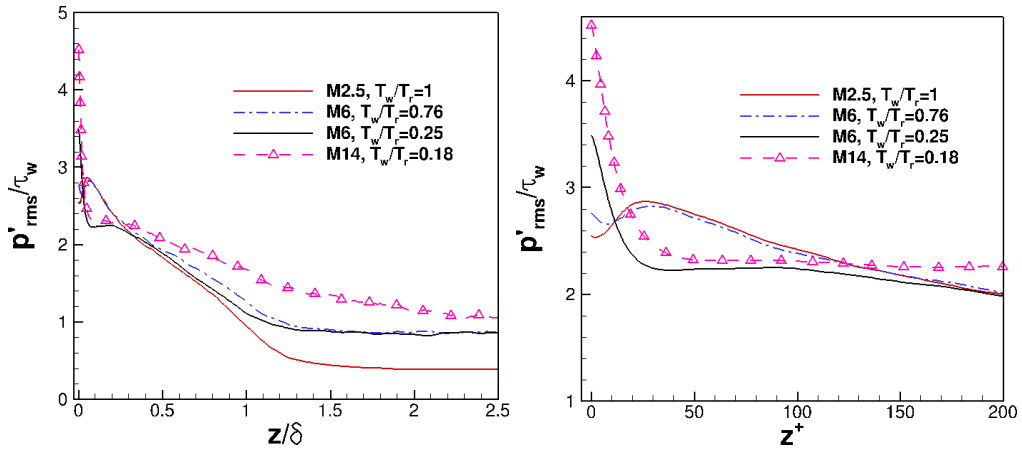

(a) Outer scale (b) Inner scale

Figure 6. Wall-normal distributions of the normalized rms pressure fluctuation p'_{rms}/τ_w. (a) Outer scale; (b) Innter scale.

To see the distribution of energy among various frequencies of the pressure fluctuation, Figure 7 shows the scaled pre-multiplied pressure spectrum at multiple selected heights. The pressure spectra at the surface involve a broadband peak at $f\delta/U_\infty \approx 2$. As the location of interest moves away from the wall, the spectrum peak shifts to lower frequencies. Significant reduction in the peak frequency f_{pk} occurs within the inner layer (including the viscous sublayer, buffer layer, and log layer), where f_{pk} is reduced approximately two fold, reaching a lower frequency of $f_{pk}\delta/U_\infty \approx 1$ at $z/\delta = 0.1$. The near-wall region with a rapid reduction in f_{pk} nearly coincides with the region where the rms of pressure undergoes a rapid reduction in magnitude (Figure 6). As it moves farther away from the wall into the outer layer, the change in the peak frequency f_{pk} becomes less rapid. In the free stream, where the the pressure signal is predominantly acoustic, the peak of the pre-multiplied spectrum is centered at a frequency of $f\delta/U_\infty \approx 0.6$, which is more than three times lower than that of the pressure spectrum at the wall, indicating that the characteristic frequency of acoustic mode is significantly lower than that of the vortical fluctuation close to the surface. The overlap between the pressure spectrum at $z/\delta = 1.57$ and that at $z/\delta = 2.27$ suggests that f_{pk} is insensitive to the wall-normal distance in the free stream at least within a short distance from the boundary-layer edge.

An indicator for the significance of compressibility effects is the turbulent Mach number M_t, defined by

$$M_t = \frac{(\overline{u'_i u'_i})^{1/2}}{\overline{a}}$$

Figure 8a shows that the magnitude of M_t increases significantly with increasing freestream Mach number. The peak value of M_t increases from approximately 0.28 for Case M2p5 to 0.68 for Case M14Tw018. The increase in M_t is partially due to wall cooling, as wall cooling reduces $\overline{a}$. In the meantime, the peak location of M_t is shifted farther away from the wall as the wall temperature decreases. A similar indicator for the direct compressibility effects is the fluctuating Mach number, M'_{rms}, which is the RMS fluctuation of the Mach number and thereby includes fluctuations in both the velocity and the temperature. Figure 8b shows that the peak value of M'_{rms} reaches a value as high as 2.1 for Case M14Tw018. Unlike the distribution of M_t, the fluctuating Mach number develops a peak near the middle of the boundary layer where both the velocity and temperature fluctuations are important.

$M_t = 0.3$ is the commonly believed threshold above which compressibility effects become important for turbulence behavior.[39] The large values of M_t and M'_{rms} for Case M14Tw018, combined with observable regions of eddy shocklets within the boundary layer (Figure 3), might indicate a non-negligible effect of

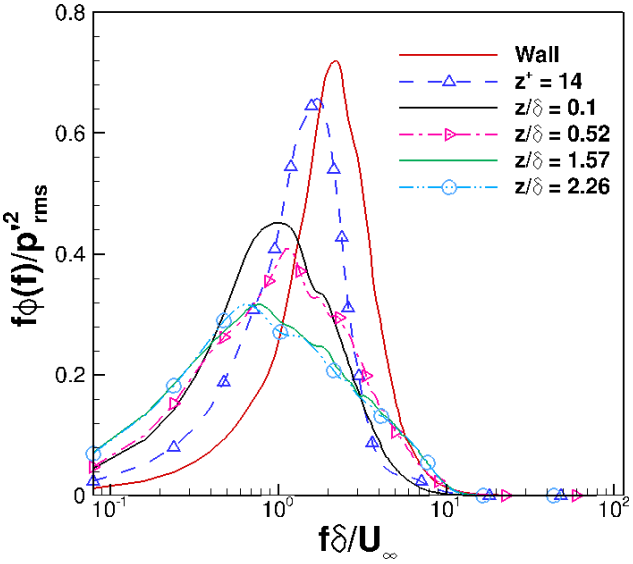

Figure 7. Pre-multiplied power spectrum of pressure signals at selected heights above the wall. The pressure spectrum is normalized so that the area under each curve is equal to unity. At the flow conditions of interest, $f\delta/U_\infty = 1$ corresponds to a dimensional frequency of $f = 29.2$ kHz.

intrinsic compressibility on flow dynamics. However, more detailed analysis is still necessary to probe and quantify the effects of intrinsic compressibility on turbulence statistics and structures.

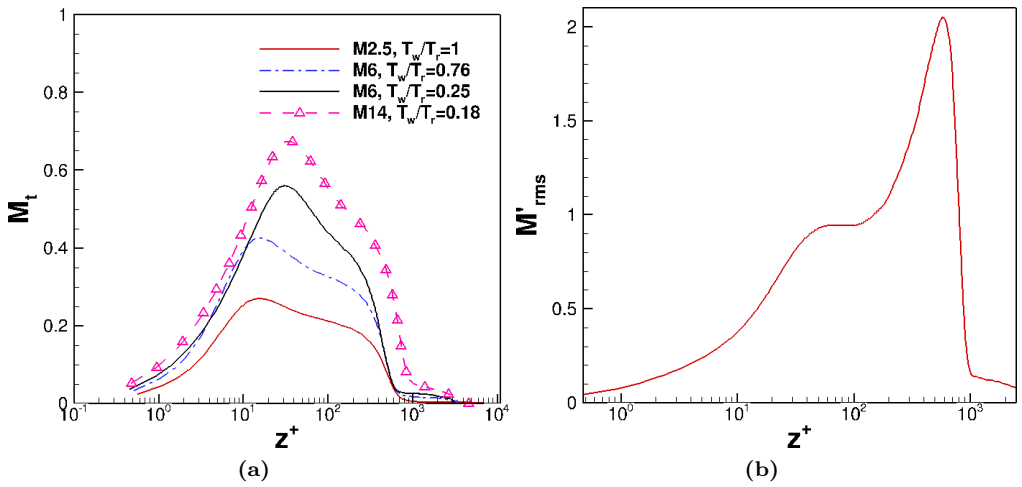

Figure 8. The distribution of (a) turbulence Mach number and (b) fluctuating Mach number.

B. Characteristics of Fluctuating Wall Quantities

Table 3 shows several mean and fluctuating wall quantities for various DNS cases, including the skin friction, the Stanton number C_h, the Reynolds analogy factor $2C_h/C_f$, and the fluctuating pressure, wall shear stress, and surface heat flux. The prediction of skin friction coefficient by the van Driest II theory,[40] $(C_f)_{VD}$, is also included and compared with the DNS calculated result. It it shown that DNS calculated skin frictions are within 5% of the van Driest II prediction for all cases. In addition, the Reynolds analogy factor $2C_h/C_f$ is close to unity, which are within the uncertainty of the experimental measurement of heat transfer,[41] indicating the validity of Reynolds analogy for turbulent boundary layers in the high-Mach-number, cold-wall regime.

In terms of the fluctuating wall quantities, Table 3 shows large fluctuation amplitudes relative to the mean value. For example, the rms of fluctuating surface pressure $p'_{w,rms}$, wall shear stress $\tau_{w,rms}$, and

heat flux $q'_{w,rms}$ are equal to approximately 24%, 53%, and 67% of the surface mean, respectively, for Case M14Tw018.

The validity of Reynolds analogy can further be demonstrated by comparing the spectra of fluctuating wall quantities. Figure 9 shows the pre-multiplied power spectrum for p'_w, τ'_w, and q'_w for Case M14Tw018. The spectra for all the fluctuating quantities at the surface involve a broadband peak at the same frequency of $f\delta/U_\infty \approx 2$. A match in the dominant frequency among wall fluctuating quantities might indicate that the fluctuations in p_w, τ_w, and q'_w are associated with similar near-wall turbulence events or are the footprints of common near-wall coherent structures.

Table 3. Mean and fluctuating wall parameters for various DNS cases.

Case	C_f ($\times 10^{-3}$)	$(C_f)_{VD}$ ($\times 10^{-3}$)	C_h ($\times 10^{-3}$)	$2C_h/C_f$	$p'_{w,rms}/\overline{p}_w$	$\tau'_{w,rms}/\tau_w$	$q'_{w,rms}/\overline{q}_w$	$p'_{w,rms}/\tau_w$
M2p5	2.30	2.24	NA	NA	0.026	0.41	NA	2.55
M6Tw076	1.07	0.97	0.67	1.25	0.065	0.42	0.94	2.76
M6Tw025	1.76	1.79	1.14	1.29	0.14	0.46	0.54	3.49
M14Tw018	0.46	0.44	0.34	1.47	0.24	0.53	0.67	4.41

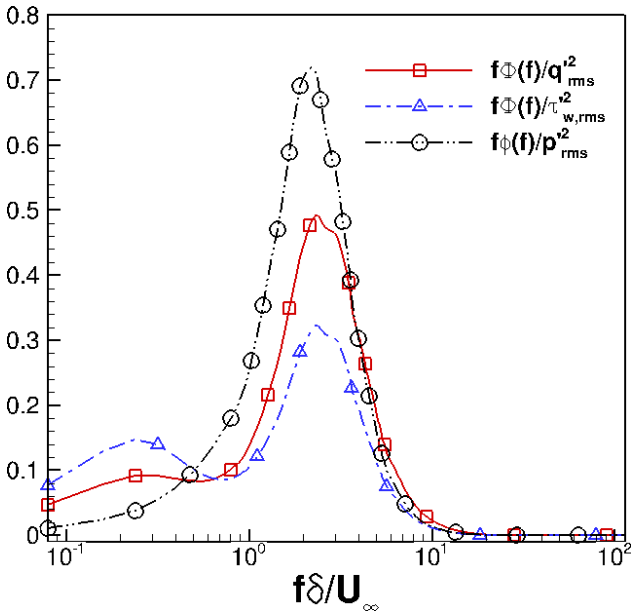

Figure 9. Pre-multiplied power spectrum of fluctuating wall signals at the wall for Case M14Tw018.

C. Characteristics of Freestream Fluctuations

Table 4 and Table 5 list the freestream values of several fluctuating flow variables at $z/\delta = 2.26$ and $z/\delta = 2.94$, respectively, for Case M14Tw018. The magnitude of freestream fluctuation decays slowly with wall-normal distance. For each freestream location, the fluctuations in thermodynamic variables are stronger than the velocity fluctuations. The rms pressure fluctuations are approximately 6.3% of the mean pressure value. The data in Tables 4 and 5 also show that $s'_{rms}/R << p'_{rms}/\overline{p}$, and by using the values listed in Tables 4 and 5, the following isentropic relations are satisfied

$$\frac{T'_{rms}}{\overline{T}} \approx \frac{\gamma-1}{\gamma}\frac{p'_{rms}}{\overline{p}}$$

$$\frac{\rho'_{rms}}{\overline{\rho}} \approx \frac{1}{\gamma}\frac{p'_{rms}}{\overline{p}}$$

indicating that the freestream fluctuations are nearly isentropic and the contribution from the entropy mode is minimal. The relative importance of acoustic mode and vorticity mode in the freestream can be demonstrated by the ratio of dilatation variance $\overline{(\partial u_i/\partial x_i)'^2}$ and vorticity variance $\overline{\Omega_i'\Omega_i'}$, which are representative of the acoustic and vorticity mode, respectively. The large value of $\overline{(\partial u_i/\partial x_i)'^2}/\overline{\Omega_i'\Omega_i'}$ implies the dominance of acoustic mode over the vorticity mode in the free stream.

Table 4. The disturbance field at $z/\delta = 2.26$ for Case M14Tw018.

$u'_{rms}/\overline{u}$	$v'_{rms}/\overline{u}$	$w'_{rms}/\overline{u}$	$p'_{rms}/\overline{p}$	$\rho'_{rms}/\overline{\rho}$	$T'_{rms}/\overline{T}$
1.3435×10^{-3}	1.2036×10^{-3}	2.4906×10^{-3}	5.8779×10^{-2}	4.1778×10^{-2}	1.6652×10^{-2}
$(\rho u)'_{rms}/\overline{\rho u}$	$T'_{t,rms}/\overline{T}_t$	$p'_{t,rms}/\overline{p}_t$	$\overline{(\partial u_i/\partial x_i)'^2}/\overline{\Omega_i'\Omega_i'}$	s'_{rms}/R	
4.1094×10^{-2}	2.3660×10^{-3}	8.4239×10^{-3}	1727	1.2483×10^{-3}	
$\overline{u'p'}/u'_{rms}p'_{rms}$	$\overline{v'p'}/v'_{rms}p'_{rms}$	$\overline{w'p'}/w'_{rms}p'_{rms}$	$\overline{\rho'p'}/\rho'_{rms}p'_{rms}$	$\overline{T'p'}/T'_{rms}p'_{rms}$	
-0.5166	-0.01126	0.9679	1	1	

Table 5. The disturbance field at $z/\delta = 2.94$ for Case M14Tw018.

$u'_{rms}/\overline{u}$	$v'_{rms}/\overline{u}$	$w'_{rms}/\overline{u}$	$p'_{rms}/\overline{p}$	$\rho'_{rms}/\overline{\rho}$	$T'_{rms}/\overline{T}$
1.1108×10^{-3}	9.8286×10^{-4}	2.1401×10^{-3}	4.9762×10^{-2}	3.5405×10^{-2}	1.4119×10^{-2}
$(\rho u)'_{rms}/\overline{\rho u}$	$T'_{t,rms}/\overline{T}_t$	$p'_{t,rms}/\overline{p}_t$	$\overline{(\partial u_i/\partial x_i)'^2}/\overline{\Omega_i'\Omega_i'}$	s'_{rms}/R	
3.4742×10^{-2}	1.9470×10^{-3}	6.8824×10^{-3}	2441	6.1889×10^{-4}	
$\overline{u'p'}/u'_{rms}p'_{rms}$	$\overline{v'p'}/v'_{rms}p'_{rms}$	$\overline{w'p'}/w'_{rms}p'_{rms}$	$\overline{\rho'p'}/\rho'_{rms}p'_{rms}$	$\overline{T'p'}/T'_{rms}p'_{rms}$	
-0.5955	0.02443	0.9820	1	1	

Figure 10a shows a comparison of pre-multiplied frequency spectrum of pressure fluctuations at multiple freestream locations for Case M14Tw018. Good convergence of the pressure spectrum is shown up to $z/\delta = 3.63$. The freestream pressure spectrum involves a broadband peak centered at $f\delta/U_\infty \approx 0.7$. Figure 10b further shows a comparion of pressure spectrum for various DNS cases. The dominant frequency f_{pk} shifts to higher values as the freestream Mach number increases, while the wall temperature has nearly no influence on f_{pk}.

Figure 11 shows the instantaneous pressure field in the free stream for Case M14Tw018. Similar to the previously studied Mach 2.5 and Mach 6 boundary layers,[6–8] the acoustic radiation for Case M14Tw018 consists of randomly spaced wavefronts with a finite spatial coherence. The wave angle (the angle between the wave front and the flow direction) for the eddy-Mach waves is approximate 20° for Case M14Tw018, which is smaller compared with lower Mach number cases and is consistent with the theory of eddy-Mach-wave radiation.[42]

V. Summary

Direct numerical simulation of a spatially-developing zero-pressure-gradient hypersonic turbulent boundary layer is presented for $M_\infty = 14$ and $T_w/T_r = 0.18$. The flow conditions correspond to those at the nozzle exit of the Arnold Engineering Development Center Hypervelocity Tunnel No. 9 facility. The simulation results are compared with our previous simulations at Mach 2.5 and Mach 6[6–8] to assess the influence of freestream Mach number and wall-temperature conditions on the turbulence statistics within the boundary layer and the radiation field in the free stream.

Consistent with previous studies of turbulent boundary layer at high Mach numbers, the van Driest transformation and Morkovin's scaling remain valid under this flow condition. The property of pressure fluctuations varies dramatically within the inner layer ($z/\delta \lessapprox 0.08$ or $z^+ \lessapprox 50$), both in terms of the fluctuation magnitude p'_{rms}/τ_w and the dominant frequency f_{pk} associated with the peak of the pre-multiplied pressure spectrum. p'_{rms}/τ_w undergoes a rapid reduction in magnitude with $p'_{rms}/\tau_w \approx 4.4$ at the surface and $p'_{rms}/\tau_w \approx 2.3$ at $z/\delta \approx 0.08$ ($z^+ \approx 50$). The peak of frequency spectrum of the pressure fluctuation is

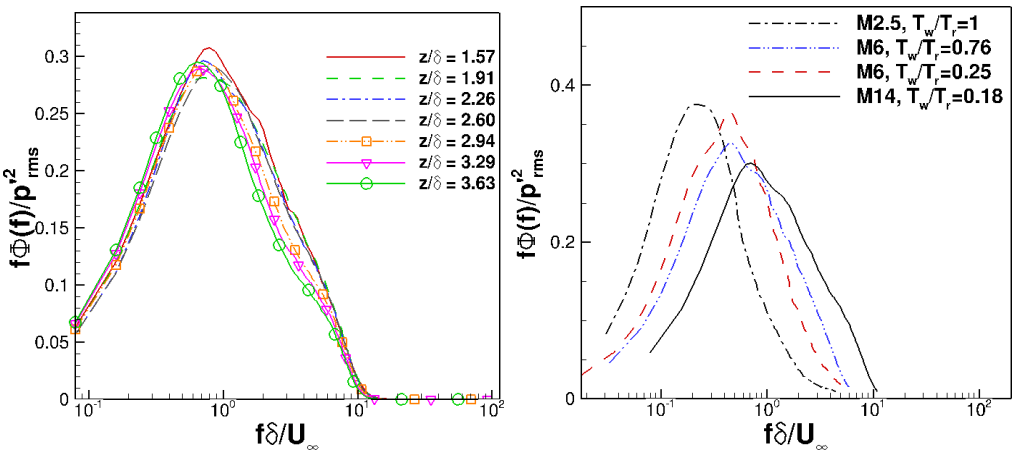

(a) (b)

Figure 10. Pre-multiplied power spectrum of pressure signals (a) at multiple freestream locations for Case M14Tw018 and (b) for various DNS cases.

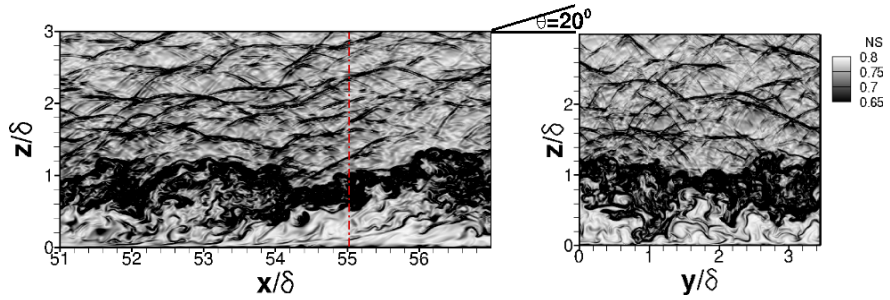

Figure 11. Numerical Schlieren visualization of a typical flow field for Case M14Tw018 in a streamwise wall-normal (x-z) plane and a spanwise wall-normal (y-z) plane. Contour levels are selected to emphasize disturbances in the free stream. The y-z plane is located at $x/\delta = 55.1$ (or $x/\delta_i = 189.2$) as indicated by the vertical dashed line. θ is the angle between the wave front and the flow direction.

$f_{pk}\delta/U_\infty \approx 2.1$ at the surface, $f_{pk}\delta/U_\infty \approx 1.0$ at $z/\delta = 0.1$, and $f_{pk}\delta/U_\infty \approx 0.7$ in the free stream.

The rms of fluctuating surface pressure $p'_{w,rms}$, wall shear stress $\tau_{w,rms}$, and heat flux $q'_{w,rms}$ is equal to approximately 24%, 53%, and 67% of the surface mean, respectively. The Reynolds analogy is valid at the surface with the Reynolds analogy factor $2C_h/C_f \approx 1.0$.

The freestream pressure signal is predominantly acoustic with a higher peak frequency f_{pk} and a shallower Mach-wave radiation angle than the Mach 2.5 and Mach 6 cases.

Acknowledgments

This material is based on the work supported by the Air Force Office of Scientific Research with Award No. FA9550-14-1-0170, managed by Dr. Rengasamy Ponnappan. The work was initiated under the support of NASA Langley Research Center under the Research Cooperative Agreement No. NNL09AA00A (through the National Institute of Aerospace). Computational resources are provided by the NASA Advanced Supercomputing Division and the DoD High Performance Computing Modernization Program.

References

[1]Fedorov, A. V., "Receptivity of a High-Speed Boundary Layer to Acoustic Disturbances," *Journal of Fluid Mechanics*, Vol. 491, 2003, pp. 101–129.

[2]Zhong, X. and Wang, X., "Direct Numerical Simulation on the Receptivity, Instability, and Transition of Hypersonic Boundary Layers," *Annu. Rev. Fluid Mech.*, Vol. 44, 2012, pp. 527–561.

[3]Laufer, J., "Some Statistical Properties of the Pressure Field Radiated by a Turbulent Boundary Layer," *Physics of Fluids*, Vol. 7, No. 8, 1964, pp. 1191–1197.

[4]Donaldson, J. and Coulter, S., "A Review of Free-Stream Flow Fluctuation and Steady-State Flow Quality Measurements in the AEDC/VKF Supersonic Tunnel A and Hypersonic Tunnel B," AIAA Paper 95-6137, 1995.

[5]Schneider, S. P., "Effects of High-Speed Tunnel Noise on Laminar-Turbulent Transition," *Journal of Spacecraft and Rockets*, Vol. 38, No. 3, 2001, pp. 323–333.

[6]Duan, L., Choudhari, M. M., and Wu, M., "Numerical Study of Pressure Fluctuations due to a Supersonic Turbulent Boundary Layer," *Journal of Fluid Mechanics*, Vol. 746, 2014, pp. 165–192.

[7]Duan, L. and Choudhari, M. M., "Numerical Study of Pressure Fluctuations due to a Mach 6 Turbulent Boundary Layer," *AIAA Paper 2013-0532*, 2013.

[8]Duan, L. and Choudhari, M. M., "Analysis of Numerical Simulation Database for Pressure Fluctuations Induced by High-Speed Turbulent Boundary Layers," *AIAA Paper 2014-2912*, 2014.

[9]Harvey, W. D., "Influence of Free-Stream Disturbances on Boundary-Layer Transition," *NASA Technical Memorandum 78635*, 1978.

[10]Bounitch, A., Lewis, D. R., and Lafety, J. F., "Improved Measurement of "Tunnel Noise" Pressure Fluctuations in the AEDC Hypervelocity Wind Tunnel No. 9," *AIAA Paper 2011-1200*, 2011.

[11]Roy, C. J. and Blottner, F. G., "Review and Assessment of Turbulence Models for Hypersonic Flows," *Progress in Aerospace Sciences*, Vol. 42, 2006, pp. 469–530.

[12]Duan, L., Beekman, I., and Martín, M. P., "Direct Numerical Simulation of Hypersonic Turbulent Boundary Layers. Part 3: Effect of Mach Number," *Journal of Fluid Mechanics*, Vol. 672, 2011, pp. 245–267.

[13]Duan, L., Beekman, I., and Martín, M. P., "Direct Numerical Simulation of Hypersonic Turbulent Boundary Layers. Part 2: Effect of Wall Temperature," *Journal of Fluid Mechanics*, Vol. 655, 2010, pp. 419–445.

[14]Priebe, S. and Martín, M. P., "Direct Numerical Simulation of a Hypersonic Turbulent Boundary Layer on a Large Domain," AIAA Paper 2011-3432, 2011.

[15]Sahoo, D., Ringuette, M. J., and Smits, A. J., "Experimental Investigation of a Hypersonic Turbulent Boundary Layer," *AIAA Paper 2009-0780*, 2009.

[16]Williams, O. J. and Smits, A. J., "Application of PIV to the Measurement of Hypersonic Turbulence," *16th Int. Symp. on Applications of Laser Techniques to Fluid Mechanics*, Lisbon, Portugal, 2012.

[17]Brooks, J., Gupta, A., Smith, M. S., and Marineau, E. C., "Development of Non-Intrusive Velocity Measurement Capabilities at AEDC Tunnel 9," *AIAA Paper 2014-1239*, 2014.

[18]Wu, M. and Martín, M. P., "Direct numerical simulation of supersonic boundary layer over a compression ramp," *AIAA Journal*, Vol. 45, No. 4, 2007, pp. 879–889.

[19]Jiang, G. S. and Shu, C. W., "Efficient Implementation of Weighted ENO Schemes," *Journal of Computational Physics*, Vol. 126, No. 1, 1996, pp. 202–228.

[20]Taylor, E. M., Wu, M., and Martín, M. P., "Optimization of Nonlinear Error Sources for Weighted Non-Oscillatory Methods in Direct Numerical Simulations of Compressible Turbulence," *Journal of Computational Physics*, Vol. 223, No. 1, 2006, pp. 384–397.

[21]Williamson, J., "Low-Storage Runge-Kutta Schemes," *Journal of Computational Physics*, Vol. 35, No. 1, 1980, pp. 48–56.

[22]Xu, S. and Martín, M. P., "Assessment of Inflow Boundary Conditions for Compressible Turbulent Boundary Layers," *Physics of Fluids*, Vol. 16, No. 7, 2004, pp. 2623–2639.

[23]Morgan, B., Larsson, J., Kawai, S., and Lele, S. K., "Improving Low-Frequency Characteristics of Recycling/Rescaling Inflow Turbulence Generation," *AIAA Journal*, Vol. 49, No. 3, 2011, pp. 582–597.

[24]Simens, M. P., Jimenez, J., Hoyas, S., and Mizuno, Y., "A High-resolution Code for Turbulent Boundary Layers," *Journal of Computational Physics*, Vol. 228, No. 11, June 2009, pp. 4218–4231.

[25]Martín, M., "DNS of Hypersonic Turbulent Boundary Layers. Part I: Initialization and Comparison with Experiments," *Journal of Fluid Mechanics*, Vol. 570, 2007, pp. 347–364.

[26]Duan, L. and Martín, M. P., "Direct Numerical Simulation of Hypersonic Turbulent Boundary Layers. Part 4: Effect of High Enthalpy," *Journal of Fluid Mechanics*, Vol. 684, 2011, pp. 25–59.

[27]Thompson, K. W., "Time Dependent Boundary Conditions for Hyperbolic Systems," *Journal of Computational Physics*, Vol. 68, No. 1, January 1987, pp. 1–24.

[28]Duan, L., Choudhari, M. M., Li, F., and Wu, M., "Direct Numerical Simulation of Transition in a Swept-Wing Boundary Layer," *AIAA Paper 2013-2617*, 2013.

[29]Choudhari, M. M., Li, F., Duan, L., Chang, C.-L., Carpenter, M. H., Streett, C. L., and Malik, M. R., "Towards Bridging the Gaps in Holistic Transition Prediction via Numerical Simulations (Invited)," *AIAA Paper 2013-2718*, 2013.

[30]Guarini, S. E., Moser, R. D., Shariff, K., and Wray, A., "Direct Numerical Simulation of a Supersonic Turbulent Boundary Layer at Mach 2.5," *Journal of Fluid Mechanics*, Vol. 414, 2000, pp. 1–33.

[31]Borg, M. P. and Schneider, S. P., "Effect of Free-stream Noise on Roughness-Induced Transition for the X-51A Forebody," *Journal of Spacecraft and Rockets*, Vol. 45, No. 6, 2008, pp. 1106–1116.

[32]Welch, P. D., "The Use of Fast Fourier Transform for the Estimation of Power Spectra: A Method Based on Time Averaging Over Short, Modified Periodograms," *IEEE Trans. Audio Electroacoustics*, Vol. AU-15, 1967, pp. 70–73.

[33]Maeder, T., *Numerical investigation of supersonic turbulent boundary layers*, Ph.D. thesis, ETH, Zürich, 2000.

[34]Spalart, P. R., "Direct Simulation of a Turbulent Boundary Layer up to $Re_\theta = 1410$," *Journal of Fluid Mechanics*, Vol. 187, 1988, pp. 61–98.

[35]Maeder, T., Adams, N. A., and Kleiser, L., "Direct simulation of turbulent supersonic boundary layers by an extended temporal approach," *Journal of Fluid Mechanics*, Vol. 429, 2001, pp. 187–216.

[36]Gatski, T. B. and Erlebacher, G., "Numerical simulation of a spatially evolving supersonic turbulent boundary layer," Tech. Rep. 211934, NASA Tech. Memo., 2002.

[37]Pirozzoli, S., Grasso, F., and Gatski, T. B., "Direct numerical simulation and analysis of a spatially evolving supersonic turbulent boundary layer at M = 2.25," *Physics of Fluids*, Vol. 16, No. 3, 2004, pp. 530–545.

[38]Peltier, S. J., Humble, R. A., and Bowersox, R. D. W., "PIV of a Mach 5 Turbulent Boundary Layer over Diamond Roughness Elements," *AIAA paper 2012-3061*, 2012.

[39]Smits, A. J. and Dussauge, J. P., *Turbulent Shear Layers in Supersonic Flow*, American Institute of Physics, 2nd ed., 2006.

[40]van Driest, E. R., "The problem of aerodynamic heating," *Aeronautical Engineering Review*, Vol. 15, No. 10, 1956, pp. 26–41.

[41]Hopkins, E. J. and Inouye, M., "Evaluation of theories for predicting turbulent skin friction and heat transfer on flat plates at supersonic and hypersonic Mach numbers," *AIAA Journal*, Vol. 9, No. 6, 1971, pp. 993–1003.

[42]Phillips, O. M., "On the Generation of Sound by Supersonic Turbulent Shear Layers," *Journal of Fluid Mechanics*, Vol. 9, 1960, pp. 1–28.